Mechanics & Industry **21**, 305 (2020)

https://doi.org/10.1051/meca/2020017

Mechanics & Industry

Available online at:
www.mechanics-industry.org

Regular Article

A multiobjective optimization of journal bearing with double parabolic profiles and groove textures under steady operating conditions

Chongpei Liu[1], Ning Zhong[2], Xiqun Lu[1], and Bin Zhao[1,*]

[1] College of Power and Energy Engineering, Harbin Engineering University, Harbin, PR China
[2] Chongqing Yuejin Machinery Plant Co., Ltd, Chongqing, PR China

Received: 27 December 2019 / Accepted: 20 February 2020

Abstract. The double parabolic profiles can help journal bearing to reduce bushing edge wear, but it also reduces load carrying capacity and increases friction loss. To overcome these drawbacks, in this study, a multiobjective optimization of journal bearing with double parabolic profiles and groove textures is researched under steady operating conditions using Taguchi and grey relational analysis methods. Firstly, a lubrication model with journal misalignment, elastic deformation, asperity contact, thermal effect is established and formation cause of drawbacks is illustrated. Then, an orthogonal test with considering six factors, i.e., groove number, groove depth, groove length, axial width of double parabolic profiles, radial height of double parabolic profiles and groove location is conducted, meanwhile the effects and significances of each factor on response variables are revealed. Finally, an optimal parameters combination of six factors is determined by grey relational analysis, which gives maximum load carrying capacity and minimum friction loss. Overall, this study may give guidance on journal bearing design to enhance its tribological performance.

Keywords: Double parabolic profiles / Groove textures / Load carrying capacity / Friction loss / Multiobjective optimization

1 Introduction

Journal bearing is a critical component in practical engineering. As the journal misalignment, deformation, machining and installation errors are unavoidable, bushing edge wear is found in some applications, as illustrated in Figure 1. Earlier study [1] had shown the double parabolic profiles can reduce bushing edge wear, but it also reduces load carrying capacity and increases friction loss, which still need to be well solved.

For mechanical components, surface texturing has been widely used in the past decades to improve their contact performance [2]. Specially, effects of surface textures on performance of journal bearing also attracted wide attentions to scholars. Ji et al. [3] employed sinusoidal waves to characterize rough surface, which showed the greater roughness ratio can suppress the hydrodynamic effect of textures significantly. Hence, it is necessary to minimize roughness of textured surface. Gu et al. [4] presented a mixed lubrication model to analyze the performance of groove textured journal bearing with non-Newtonian fluid operating from mixed to hydrodynamic lubrications. Their results showed the surface texturing can increase the asperity contacts, but the contact behaviors mainly arise in first cycle of start-up process. When journal bearing works under normal operating conditions, the wear due to asperity contacts will be small. Literatures [5–10] showed the partial textures can positively affect bearing performance, but the optimal locations are some different depending on geometrical parameters and working conditions [5]. Yu [6] and Lin [7] showed the textures located at rising phase of pressure field increases load carrying capacity, while the textures located at falling phase of pressure field reduces load carrying capacity. However, Tala-Ighil et al. [8,9] showed the textures located in declining part of pressure field can generate extra hydrodynamic lift. Shinde and Pawar [10] pointed out among three partial grooving configurations ($90–180^0$, $90–270^0$, $90–360^0$), the first configuration gives the maximum pressure increase while the last configuration gives the minimum frictional power loss. Their results

* e-mail: donglizhaobin@hrbeu.edu.cn

indicate the optimal location also depends on the optimization target.

Studies mentioned above have shown the texture performance is affected by many factors, which makes it very complicated to obtain the optimal design. To address this issue, some optimization methods are adopted by researchers, including the genetic algorithm [11–13], neural network [14] and sequential quadratic programming [15], while these methods are somewhat difficult in mathematics. By contrast, Taguchi method may provide a handy way for this issue. Taguchi assumes that introducing quality concepts at design stage may be more valuable than inspection after manufacturing. Hence, Taguchi method aims to optimize process to minimize quality loss with objective functions such as "the-nominal-the-best", "the-larger-the-better", or "the-smaller-the-better" depending on experimental objectives [16]. In practical engineering, this method uses the concept of orthogonal array to reduce the numbers of experiments, which facilitates to research multi-parameters concurrently and evaluate the effects of each parameter. Some studies [17–19] have already adopted Taguchi method to optimize surface textures for journal bearing to maximize load carrying capacity, minimize side leakage and friction loss.

Despite of remarkable progress on research of surface textures, few studies have been researched the journal bearing with double parabolic profiles and groove textures. The novelty of this study is to adopt the Taguchi and grey relational analysis methods to conduct a multiobjective optimization of journal bearing with double parabolic profiles and groove textures, i.e., double parabolic profiles are applied to eliminate bushing edge wear, while groove textures are applied to overcome the negative effects of the former, such as reduced load carrying capacity and increased friction loss. The results show this study may help journal bearing to enhance its tribological performance.

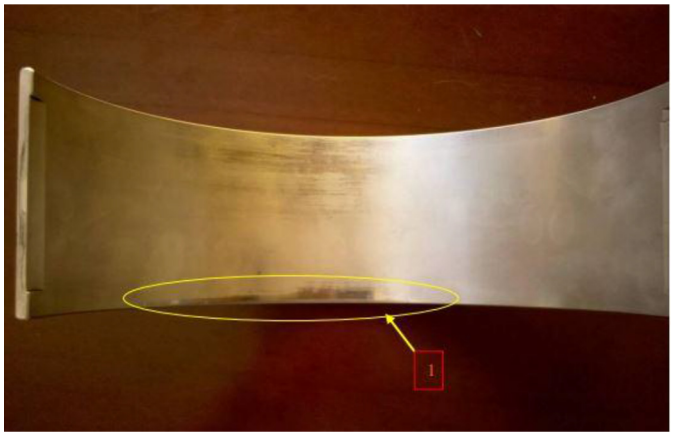

Fig. 1. The bushing edge wear.

2 Lubrication model

2.1 Geometric model

Figure 2 illustrates the layout of double parabolic profiles and groove textures investigated in this study. In Figure 2, B and d_b are the bushing width and thickness; L_y and L_z are the axial width and radial height of double parabolic profiles, whose equation can be described as $\delta_z = (L_z/L_y^2)\, y^2$; $(\theta_s - \theta_e)$, w_g, d_g, l_g and w_e, are the groove location, width, depth, length and gap, and their specific values will be introduced in Section 4.

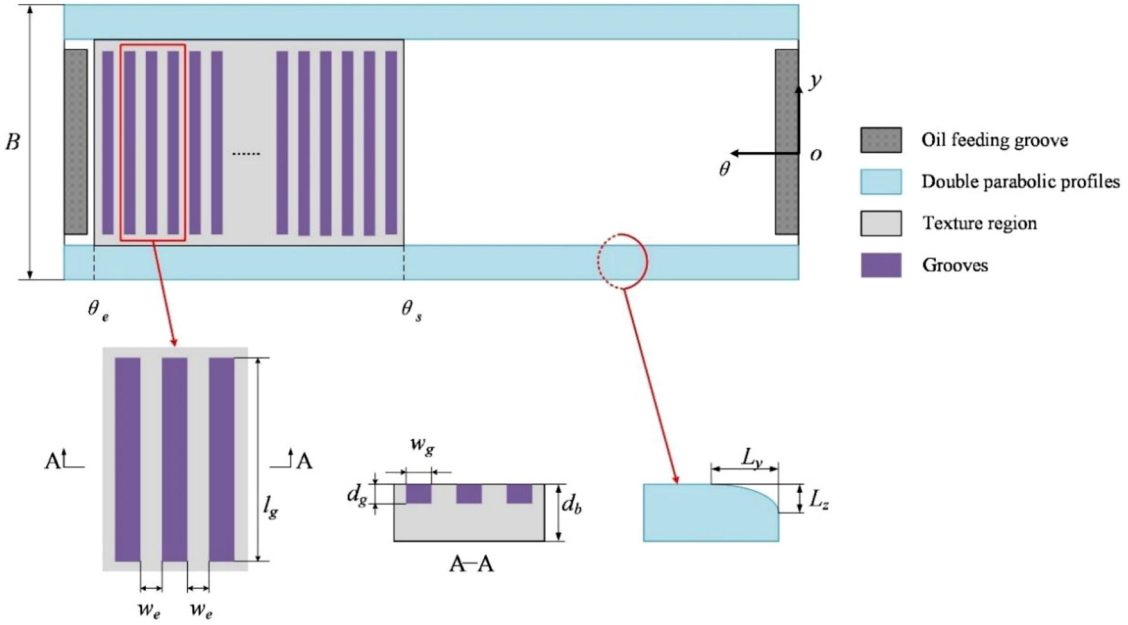

Fig. 2. Layout of double parabolic profiles and groove textures.

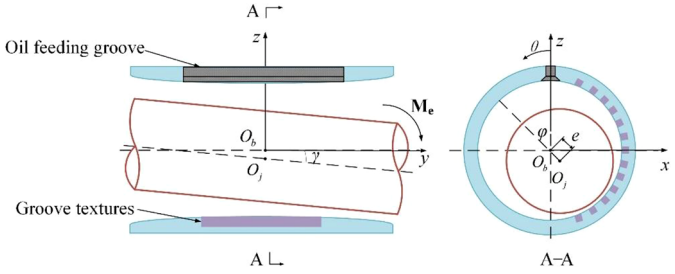

Fig. 3. A misaligned journal bearing.

2.2 Film thickness

Figure 3 illustrates a misaligned journal bearing under external moment $\mathbf{M_e}$, whose lubricating oil is supplied through the axial oil feeding groove. For simplicity, only the misalignment in vertical plane yoz is considered.

As the elastic module of journal is much higher than that of bushing, only elastic deformation of bushing surface is considered. Thus, the nominal film thickness h is

$$h = h_g + \delta_e \tag{1}$$

where h_g is the nominal film thickness without elastic deformation, which is

$$h_g = c + (e + y\tan\gamma)\cos(\theta - \varphi) + \delta_z + \delta_{tex} \tag{2}$$

where c is the radial clearance, e the eccentricity of the midplane, φ the attitude angle of the midplane, y the axial coordinate, γ the misalignment angle, δ_z the clearance added by double parabolic profiles, δ_{tex} the clearance added by groove textures. Obviously, for journal bearing with plain profile, $\delta_z = \delta_{tex} = 0$, and for journal bearing with only double parabolic profiles, $\delta_{tex} = 0$.

In this study, the elastic deformation δ_e is obtained by Winkler/Column model [20], which gives a simpler way than finite element method [21] to estimate elastic deformation and has been used in literatures [22–24]. The model assumes the local elastic deformation is only dependent on local film pressure, as expressed in equation (3)

$$\delta_e = \frac{(1+\nu)(1-2\nu)}{(1-\nu)}\frac{d}{E}p \tag{3}$$

where ν is the Poisson's ratio of alloy layer, E the elastic modulus of alloy layer, p the film pressure, d the thickness of alloy layer.

2.3 Reynolds equation

The Reynolds equation based on average flow model is utilized to determine the roughness effects on performance of journal bearing [25,26], as expressed in equation (4)

$$\frac{\partial}{\partial x}\left(\phi_x\frac{h^3}{12\mu}\cdot\frac{\partial p}{\partial x}\right) + \frac{\partial}{\partial y}\left(\phi_y\frac{h^3}{12\mu}\cdot\frac{\partial p}{\partial y}\right) = \frac{U_1+U_2}{2}\frac{\partial h_T}{\partial x} + \frac{U_1-U_2}{2}\sigma\frac{\partial \phi_s}{\partial x} + \frac{\partial h_T}{\partial t} \tag{4}$$

where μ is the viscosity of lubricating oil, p the film pressure, U_1 and U_2 the velocities of two surfaces, σ the standard deviation of combined roughness, ϕ_x, ϕ_y the pressure flow factors, ϕ_s the shear flow factor, h_T the local film thickness.

For journal bearing under steady operating conditions, equation (4) can be expressed as followed by the variable transformation $x = R\theta$

$$\frac{1}{R^2}\frac{\partial}{\partial\theta}\left(\phi_x\frac{h^3}{\mu}\cdot\frac{\partial p}{\partial\theta}\right) + \frac{\partial}{\partial y}\left(\phi_y\frac{h^3}{\mu}\cdot\frac{\partial p}{\partial y}\right) = 6\omega\frac{\partial h_T}{\partial\theta} + 6\omega\sigma\frac{\partial\phi_s}{\partial\theta} \tag{5}$$

where ω is angular velocity of journal.

2.4 Asperity contact pressure

The asperity contact model proposed by Greenwood and Tripp [27] is utilized here to estimate interaction effects of asperities, which is widely used in the analysis of rough surfaces contact of journal bearing. The asperity contact pressure P_{asp} is given by

$$P_{asp} = \frac{16\sqrt{2}\pi}{15}(\eta\beta\sigma)^2\sqrt{\frac{\sigma}{\beta}}\cdot E_c\cdot F_{2.5}(h/\sigma) \tag{6}$$

where η is the number of asperities per unit area, β the mean radius of curvature of the asperities, σ the standard derivation, E_c the composite elastic modulus, $F_{2.5}(h/\sigma)$ the Gaussian distribution function. Note the surface pattern parameter γ is assumed as 1, which means the roughness structures are isotropic.

2.5 Friction loss

It is assumed when journal bearing operates in mixed lubrication, the total friction force consists of hydrodynamic friction force arising from the shearing of lubricating oil and asperity contact friction force [28]. Hence, the total friction force f is

$$f = \int_0^B\int_0^{2\pi}\left(\frac{\mu U}{h}(\phi_f + \phi_{fs}) + \phi_{fp}\frac{h}{2R}\frac{\partial p}{\partial\theta} + \mu_{asp}\cdot p_{asp}\right)Rd\theta dy \tag{7}$$

where $U = \omega R$, ϕ_f, ϕ_{fs}, ϕ_{fp} are shear stress factors, μ_{asp} boundary friction coefficient, here $\mu_{asp} = 0.02$. The friction loss P_f can be calculated by

$$P_f = fU. \tag{8}$$

2.6 Leakage flowrate

The leakage flowrate Q_1 from front-end plane of bearing and Q_2 from rear end plane of bearings are [21]

$$\begin{cases} Q_1 = -\int_0^{2\pi} \phi_y \frac{h^3}{12\mu}\frac{\partial p}{\partial y}\Big|_{y=0} Rd\theta \\ Q_2 = -\int_0^{2\pi} \phi_y \frac{h^3}{12\mu}\frac{\partial p}{\partial y}\Big|_{y=B} Rd\theta \end{cases}. \tag{9}$$

The total leakage flowrate Q is

$$Q = |Q_1| + |Q_2|. \tag{10}$$

2.7 Thermal effect

As well known, the temperature of lubricating oil will increase and its viscosity will decrease during operations, so it is more accurate to adopt a variable viscosity model in calculation. In this study, an effective temperature is obtained based on the adiabatic flow hypothesis of lubricating oil, as shown below

$$T_e = T_i + k\frac{P_f}{Q\rho c_l} \tag{11}$$

where T_e is the effective temperature of lubricating oil, T_i the inlet oil temperature, P_f the friction loss, Q the total leakage flowrate, ρ the density of lubricating oil, c_l the specific heat of lubricating oil, k the correction factor and $k = 0.9$ [29]. This simple method avoids the complex computation of thermohydrodynamic lubrication and has been used in the literatures [24].

CD40 lubricating oil is used here and its viscosity-temperature equation can be expressed as

$$\ln\left(\frac{1}{a}\ln(1000\mu)\right) = bT_e^2 + cT_e \tag{12}$$

where the unit of μ is Pa·s, and $a = 6.163$, $b = 8.721 \times 10^{-5}$, $c = -0.0455$, respectively. Once the effective temperature is obtained, the effective viscosity can be calculated by the equation (12).

2.8 Load equilibrium

In this study, the external load is assumed as a pure moment whose direction is parallel to x axis, which only leads to a journal misalignment in vertical plane yoz. The static equilibrium of journal center can be described as

$$\mathbf{M_e} + \mathbf{M_t} = \mathbf{0} \tag{13}$$

where $\mathbf{M_e}$ is the external moment, $\mathbf{M_t}$ the resultant moment of hydrodynamic moment $\mathbf{M_{oil}}$ and asperity contact moment $\mathbf{M_{asp}}$, namely $\mathbf{M_t} = \mathbf{M_{oil}} + \boldsymbol{M}_{\mathbf{asp}}$.

The load equilibrium equations along x and z axis are

$$\begin{cases} M_{ex} + M_{tx} = 0 \\ M_{ez} + M_{tz} = 0 \end{cases} \tag{14}$$

where M_{ex} and M_{ez} are the external moment along x and z axis, M_{tx} and M_{tz} the resultant moment along x and z axis, which can be expressed as follows

$$\begin{cases} M_{tx} = M_{oilx} + M_{aspx} \\ M_{tz} = M_{oilz} + M_{aspz} \end{cases} \tag{15}$$

where M_{oilx} and M_{oilz} are the hydrodynamic moment along x and z axis, M_{aspx} and M_{aspz} the asperity contact moment along x and z axis, which can be calculated by

$$\begin{cases} M_{oilx} = +\int_0^B \int_0^{2\pi} ypR\sin\theta d\theta dy \\ M_{oilz} = -\int_0^B \int_0^{2\pi} ypR\cos\theta d\theta dy \end{cases} \tag{16}$$

$$\begin{cases} M_{aspx} = +\int_0^B \int_0^{2\pi} yp_{asp}R\sin\theta d\theta dy \\ M_{aspz} = -\int_0^B \int_0^{2\pi} yp_{asp}R\cos\theta d\theta dy \end{cases} \tag{17}$$

3 Numerical procedure and verification

Apply the finite difference method to discretize equation (5), then solve the difference equations by overrelaxation iterative method. Reynolds boundary conditions are used to determine the rupture zone of oil film, and the pressures in oil feeding groove and both bearing ends are assumed as zero. The discretized pressure can be calculated by

$$p_{i,j}^{(k_p+1)} = p_{i,j}^{(k_p)} - \omega_s \times \left[p_{i,j}^{(k_p)} - \begin{pmatrix} DD_{i,j} - CS_{i,j}\cdot p_{i+1,j}^{(k_p)} - CN_{i,j}\cdot p_{i-1,j}^{(k_p+1)} \\ -CE_{i,j}\cdot p_{i,j+1}^{(k_p)} - CW_{i,j}\cdot p_{i,j-1}^{(k_p+1)} \end{pmatrix} \Big/ CC_{i,j} \right] \tag{18}$$

where $p_{i,j}^{(k_p+1)}$ is the film pressure for node (i, j) at the (k_p+1)th iteration, $p_{i,j}^{(k_p)}$ the film pressure for node (i, j) at the k_pth iteration, ω_s the overrelaxation factor, here $\omega_s = 1.5$. $DD_{i,j}$, $CS_{i,j}$, $CN_{i,j}$, $CE_{i,j}$, $CW_{i,j}$, $CC_{i,j}$ are the difference coefficients during the pressure solution.

The film pressure convergence criteria at the k_pth iteration is given by

$$\frac{\sum_{j=1}^{n_\theta}\sum_{i=1}^{n_y}\left|p_{i,j}^{(k_p+1)}-p_{i,j}^{(k_p)}\right|}{\sum_{j=1}^{n_\theta}\sum_{i=1}^{n_y}p_{i,j}^{(k_p+1)}} \le \varepsilon_p \tag{19}$$

where ε_p is the allowable precision of pressure solution, here $\varepsilon_p = 10^{-5}$. n_θ and n_y are the nodes numbers along circumferential and axial direction.

Based on the equation (11), the effective temperature convergence criteria at the k_tth iteration is given by

$$\frac{\left|T_e^{(k_t+1)}-T_e^{(k_t)}\right|}{T_e^{(k_t+1)}} \le \varepsilon_t \tag{20}$$

where ε_t is the allowable precision of effective temperature solution, here $\varepsilon_t = 10^{-4}$.

When journal bearing operates in steady operations, it can be assumed the sum of hydrodynamic and asperity contact moments is approximately equal to the external moment, specifically, the motion of journal can be obtained by correcting eccentricity ratio ε ($\varepsilon = e/c$), attitude angle φ and misalignment angle γ. The correction strategies can be expressed as follows

$$\varphi = \varphi + \omega_\varphi \arctan\left(\frac{M_{tx}}{M_{tz}}\right) \tag{21}$$

$$\begin{cases} \varepsilon = \varepsilon - \omega_\varepsilon\left(\dfrac{M_t}{M_e}-1\right)\left(\dfrac{M_t}{M_e}\ge 1\right) \\ \varepsilon = \varepsilon + \omega_\varepsilon\left(1-\dfrac{M_t}{M_e}\right)\left(\dfrac{M_t}{M_e}< 1\right) \end{cases} \tag{22}$$

$$\begin{cases} \gamma = \gamma - \omega_\gamma\left(\dfrac{M_t}{M_e}-1\right)\left(\dfrac{M_t}{M_e}\ge 1\right) \\ \gamma = \gamma + \omega_\gamma\left(1-\dfrac{M_t}{M_e}\right)\left(\dfrac{M_t}{M_e}< 1\right) \end{cases} \tag{23}$$

where M_e is the amplitude of $\mathbf{M_e}$, M_t is the amplitude of $\mathbf{M_t}$, ω_φ, ω_ε, ω_γ are the correction factors of φ, ε, γ, and $\omega_\varphi = 0.9$, $\omega_\varepsilon = 10^{-2}$, $\omega_\gamma = 10^{-5}$, respectively.

As mentioned above, the external load is a pure moment whose direction is parallel to the x axis. Accordingly, the equilibrium convergence criteria can be given by

$$\left|\frac{M_{tx}}{M_{tz}}\right| \le err_{xz} \tag{24}$$

$$\frac{|M_t - M_e|}{M_e} \le err_M \tag{25}$$

where err_{xz} and err_M are allowable precisions for the equilibrium calculation, here $err_{xz} = 10^{-3}$, $err_M = 10^{-3}$.

The whole computational process is shown in Figure 4, and the programing platform is Intel Core i7-4790 at 3.6GHz with 32GB RAM.

Before the following analysis, it is necessary to validate the model. The calculated pressures are compared with Ferron's experimental results [30], as illustrated in Figure 5. The comparisons show the calculated results agree well with the experimental ones, which confirms the validity of this model.

4 Results and discussions

The detailed parameters of the journal bearing investigated in this study are listed in Table 1.

Mesh refinement analysis is conducted based on the journal bearing with plain profile. Various mesh schemes and corresponding minimum film thickness ($h_{\min}$) are listed in Table 2. It can be seen that $h_{\min}$ is converged when the mesh is 1441×181. Considering the solving time and accuracy, 1441×181 mesh is adopted.

Here one typical case is conducted to prove the bushing edge wear can be reduced by double parabolic profiles. For journal bearing with double parabolic profiles, the chosen values of axial width L_y and radial height L_z are 10 mm and 6 μm, and the relative variation of each performance parameter is defined as

$$\delta_{dpp}X = \frac{X_{dpp} - X_{pp}}{X_{pp}} \times 100\% \tag{26}$$

where $\delta_{dpp}X$ is the relative variation of parameter X, pp means plain profile and dpp means double parabolic profiles. Note in this study, the maximum film pressure ($P_{\max}$) is used to indirectly reflect the variations of load carrying capacity, smaller $P_{\max}$ means better load carrying capacity and vice versa.

The comparison results are listed in Table 3. It can be observed that although the ε and γ both increase to some extent, the $h_{\min}$ has sharply increased and the P_{aspmax} has reduced to zero in dpp case, which confirms its validity in term of reducing edge wear. Note φ has reduced a little, this variation trend indicates the bearing stability is also improved as the dpp reduces effective bearing width, which agrees with the common sense that using short bearing is favorable for stability improvement. However, the load carrying capacity is reduced as the dpp leads to a less capacity area. Hence, greater $P_{\max}$ is generated and hydrodynamic friction force also increases which causes greater P_f. It is obvious that Q is increased as the dpp increases the film pressure gradient at bushing edge, so the comprehensive effects of greater P_f and Q lead to a tiny change of T_e based on equation (11).

Figure 6 illustrates the variations of film thickness and pressure between pp and dpp case, in Figure 6a, $\Delta h = h_{dpp} - h_{pp}$, and in Figure 6b, $\Delta P = P_{dpp} - P_{pp}$. It can be seen that, compared with pp case, the dpp case presents thicker oil film at bushing edge, which avoids the asperity contacts between journal and bushing surfaces, so the asperity contact pressure reduces to zero. However, in the region away from bushing edge, the oil film in dpp case is thinner

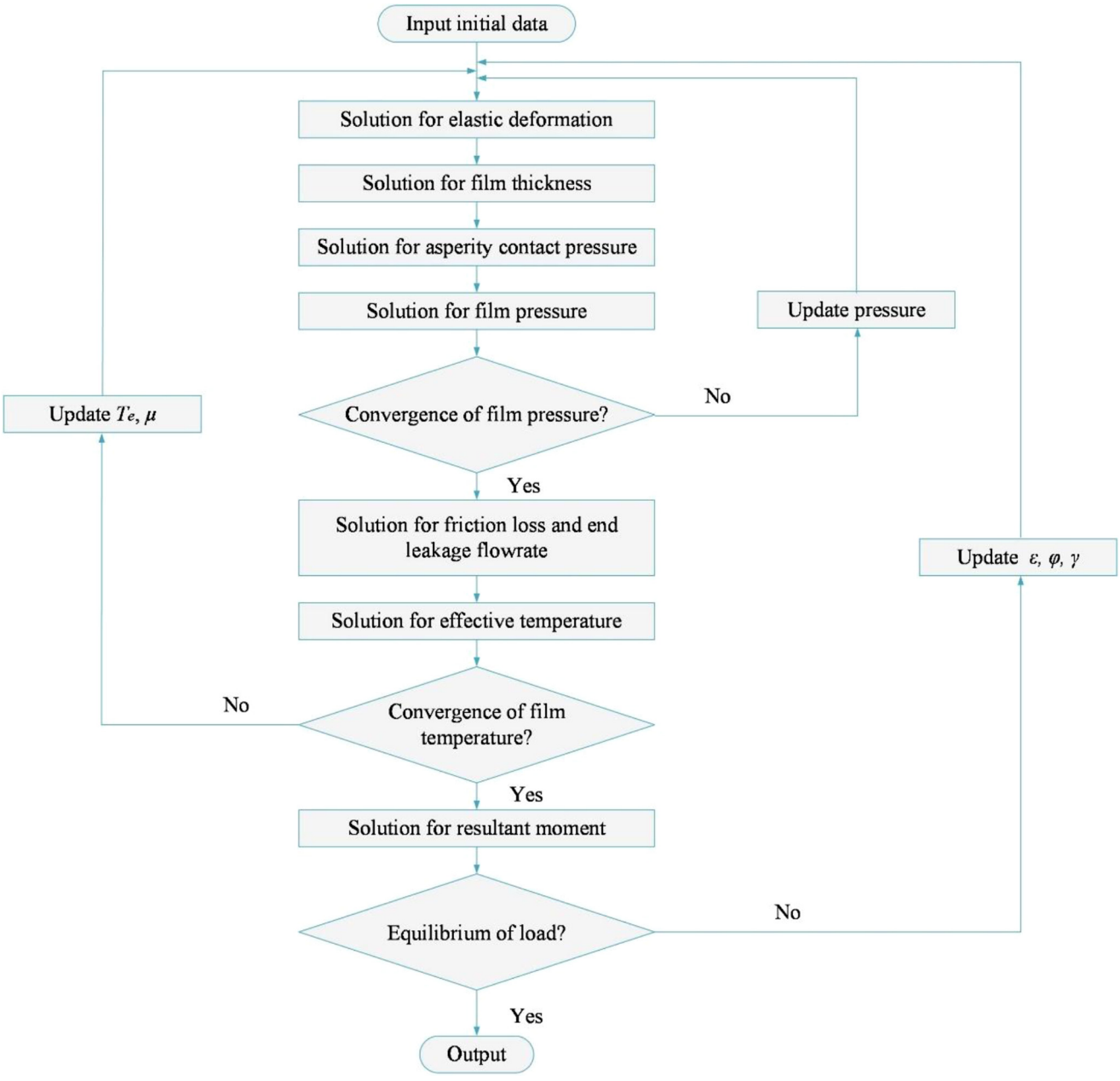

Fig. 4. Flow chart of the computational process.

than that in pp case, which causes greater film pressure here, i.e., the dpp can move the film pressure peak to inside region.

As mentioned above, although dpp can reduce bushing edge wear, it also reduces load carrying capacity and increases friction loss. The main motivation of this study is to overcome these drawbacks by groove textures, as illustrated in Figure 2. Considering the journal bearing with double parabolic profiles and groove textures (dppgt), six factors are involved in the analysis: groove number n_g, depth d_g, length l_g, axial width of dpp L_y, radial height of dpp L_z, and location $(\theta_s - \theta_e)$. Three levels for each factor are listed in Table 4. Note the total area of groove textures, $S_g = w_g \times l_g \times n_g$, is constant, while the groove width w_g, gap w_e, and number n_g are different. The values of w_g and w_e for corresponding n_g are listed in Table 5.

Clearly the study of six factors at three optional levels needs 3 [6] simulation tests if full factorial designs are implemented. To reduce the computing cost, Taguchi method with orthogonal array L_{18} is adopted here, as shown in Table 6. L_{18} is commonly used and it is more concise than L_{27} array.

As we are mainly concerned with load carrying capacity and friction loss, only the results of $P_{\max}$ and P_f are given in Table 7. Note reference group are the results of dpp case ($L_y = 5$, 10, 15 mm, $L_z = 3$, 6, 9 μm, totally 9 cases, each case will be repeated twice).

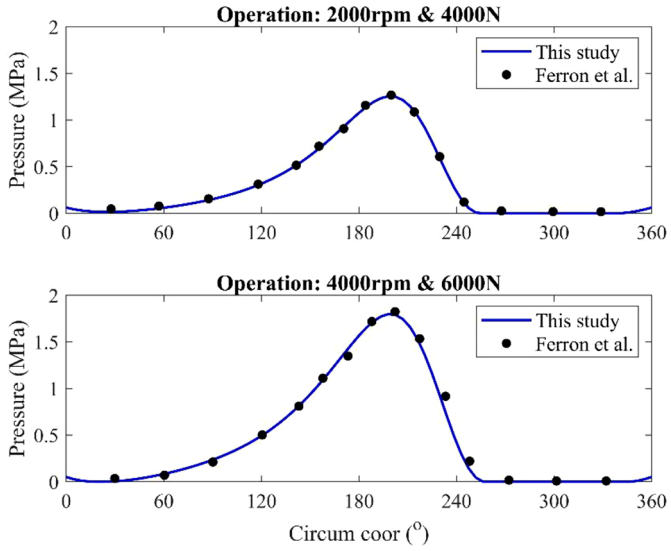

Fig. 5. Comparisons with Ferron's experimental results [30].

Table 1. Detailed parameters of the journal bearing.

Parameters	Values
Lubricating oil	CD40
Oil feeding temperature (°C)	70
Bearing diameter D (mm)	230
Bearing width B (mm)	90
Bearing bushing thickness d_b (mm)	5
Radial clearance c (mm)	0.14
Oil feeding groove (°)	18
Standard deviations of the roughness of the bearing surface σ_b (μm)	0.8
Standard deviations of the roughness of the journal surface σ_j (μm)	0.4
Elastic modulus of copper-lead-tin alloy layer E_a (GPa)	97
Poisson's ratio of copper-lead-tin alloy layer ν_a	0.3
Thickness of alloy layer d (mm)	1
External moment M_e (Nm)	2000
Rotary speed (rpm)	1080

Table 2. Mesh schemes for mesh refinement analysis.

Scheme	1	2	3	4	5
$n_\theta \times n_y$	721×121	1081×151	1441×181	1441×211	1801×211
$h_{\min}$ (μm)	1.9417	1.9347	1.9095	1.9103	1.8974

Table 3. Comparisons between journal bearing with plain profile (pp) and double parabolic profiles (dpp).

Parameters	pp	dpp	$\delta_{\text{dpp}}X$ (%)
Eccentricity ration of midplane ε	0.9167	0.9263	+1.05
Attitude angle of midplane φ(°)	189.7093	189.5775	–0.07
Misalignment angle $\gamma(10^{-2^\circ})$	1.2416	1.2968	+4.45
Min. film thickness $h_{\min}$ (μm)	1.9095	3.5935	+88.20
Max. asperity contact pressure $P_{asp\max}$ (MPa)	0.6644	0	–100.00
Max. film pressure $P_{\max}$ (MPa)	60.0312	68.1382	+13.51
Friction loss P_f (W)	4130.5236	4273.4494	+3.46
Leakage flowrate Q (10^{-4} m^3/s)	1.2720	1.3007	+2.26
Effective temperature T_e (°C)	86.6712	86.8673	+0.23

As can be seen from Table 7, compared with reference cases, the groove textures show positive effects only in No. 3, 4, 8, 11, 13 and 18 tests (shown in bold). Take the No. 8 test to explain this phenomenon: As illustrated in Figures 7 and 8, the groove textures can strengthen the hydrodynamic effect of lubricating oil and generate extra local pressure at the downstream of film pressure filed, which increases the load carrying capacity. Meanwhile, the friction force arising from the shearing of oil reduces with thicker oil film, which causes less friction loss. Note the groove locations of these six tests are all 200°–350°, which indicates the proper groove location is beneficial to performance enhancement.

While for the remaining tests, the groove textures show negative effects on either load carrying capacity or friction loss compared with reference cases. Take No. 5 and 15 tests

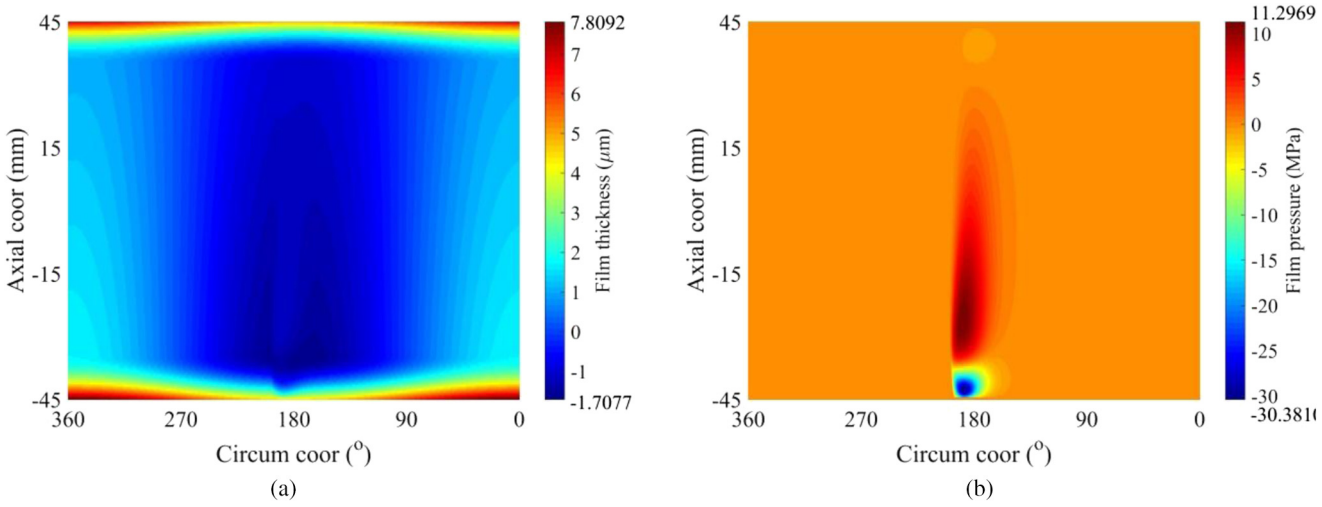

Fig. 6. (a) Differences Δh, (b) Differences ΔP between pp and dpp cases.

Table 4. Six control factors and their optional levels.

Factors	Level 1	Level 2	Level 3
n_g	120	60	30
d_g (μm)	10	15	20
l_g (mm)	40	50	60
L_y (mm)	5	10	15
L_z (μm)	3	6	9
θ_s–θ_e(°)	180–330	190–340	200–350

Table 5. Groove sizes for their optional levels.

Groove numbers n_g	120	60	30
Groove widths w_g (mm)	1.5	3.0	6.0
Groove gaps w_e (mm)	1.0	2.0	4.0

Table 6. Orthogonal array L18.

Test No.	n_g	d_g (μm)	l_g (mm)	L_y (mm)	L_z (μm)	θ_s–θ_e(°)
1	120	10	40	5	3	180–330
2	120	15	50	10	6	190–340
3	120	20	60	15	9	200–350
4	60	10	40	10	6	200–350
5	60	15	50	15	9	180–330
6	60	20	60	5	3	190–340
7	30	10	50	5	9	190–340
8	30	15	60	10	3	200–350
9	30	20	40	15	6	180–330
10	120	10	60	15	6	190–340
11	120	15	40	5	9	200–350
12	120	20	50	10	3	180–330
13	60	10	50	15	3	200–350
14	60	15	60	5	6	180–330
15	60	20	40	10	9	190–340
16	30	10	60	10	9	180–330
17	30	15	40	15	3	190–340
18	30	20	50	5	6	200–350

Table 7. Results of orthogonal tests and reference group.

Test No.	Orthogonal tests		Reference group	
	P_{max} (MPa)	P_f (W)	P_{max} (MPa)	P_f (W)
1	69.4134	4244.7385	63.2395	4192.0197
2	73.3438	4173.0918	68.1382	4273.4494
3	**73.6209**	**4149.3208**	**73.6402**	**4353.0359**
4	**67.9519**	**4217.0836**	**68.1382**	**4273.4494**
5	157.6918	4239.6102	73.6213	4353.0359
6	115.3453	3643.9945	63.2395	4192.0197
7	68.4509	4238.9667	66.8922	4257.0855
8	**62.8481**	**4113.0399**	**64.0726**	**4207.6524**
9	123.7151	4366.6101	68.7591	4283.2996
10	77.3296	4250.6529	68.7591	4283.2996
11	**66.8692**	**4155.7142**	**66.8922**	**4257.0855**
12	72.1152	4214.6034	64.0726	4207.6524
13	**63.5710**	**4124.5873**	**63.9085**	**4205.7407**
14	147.5468	4004.2271	65.4839	4233.6927
15	147.6417	3877.2633	71.4743	4318.6635
16	69.5520	4625.5756	71.4743	4318.6635
17	64.3493	4202.2618	63.9085	4205.7407
18	**64.5257**	**4167.0737**	**65.4839**	**4233.6927**

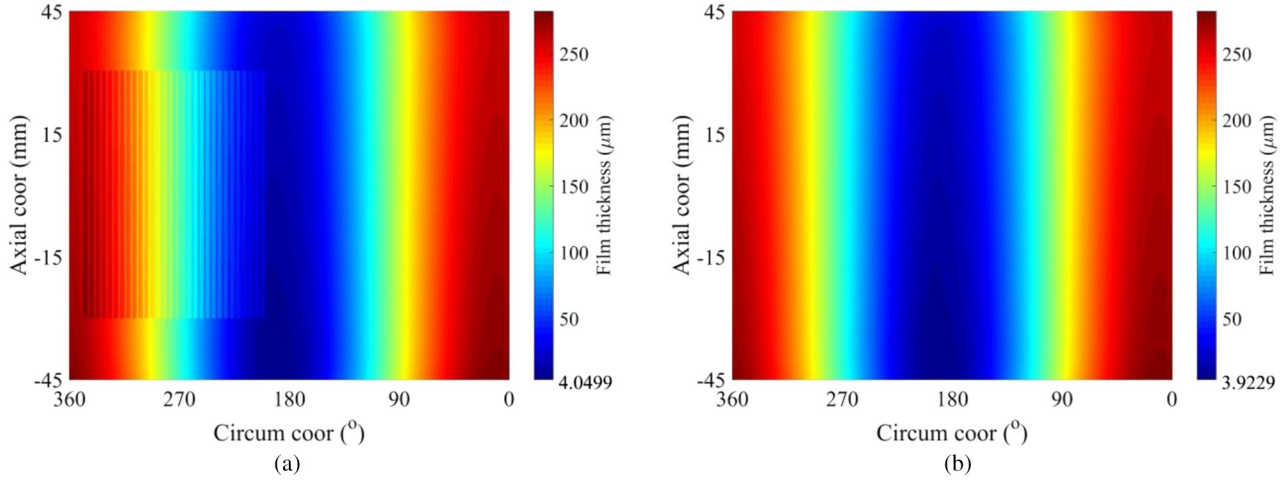

Fig. 7. (a) Film thickness of No. 8 test, (b) Film thickness of reference case 8.

to explain this phenomenon: As illustrated in Figures 9–12, the groove textures located at 180°–330° (No. 5 test) and 190°–340° (No. 15 test) increase film thickness at main loading region, so the continuous film pressure generation is destroyed and greater pressure is generated in multi-peaks at untextured land (region between two adjacent grooves). This phenomenon is more evident when the groove textures locates at 180°–330°. Meanwhile, the hydrodynamic friction loss also reduces as explained previously. Moreover, the friction loss in No. 1, 9, 12, and 16 orthogonal tests are greater than those in reference cases, coincidentally the groove locations of these four tests are all 180°–330°, which indicates the improper groove location may bring harmful effects on texture performance.

Based on the orthogonal tests, the main effect analysis and analysis of variance (ANOVA) are performed to show the effects and significance of each factor [31]. The effects of six factors on load carrying capacity (P_{max}) are illustrated in Figure 13. It is observed the optimal parameters combination is at groove number 120, depth 10 μm, length 50 mm, axial width of dpp 10 mm, radial height of dpp 3 μm, and location 200°–350°, which may give a best load

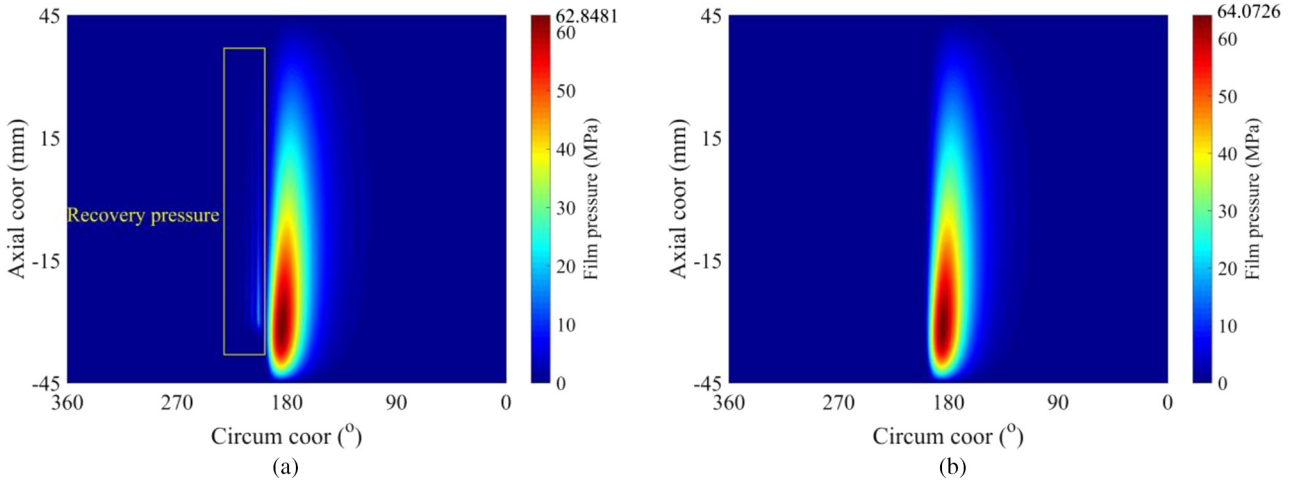

Fig. 8. (a) Film pressure of No. 8 test, (b) Film pressure of reference case 8.

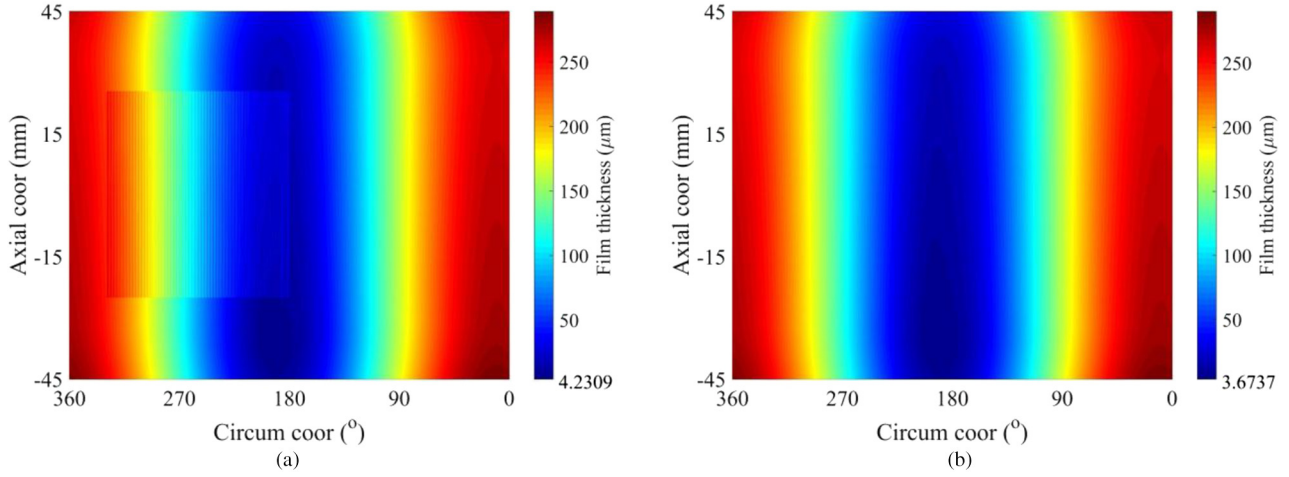

Fig. 9. (a) Film thickness of No. 5 test, (b) Film thickness of reference case 5.

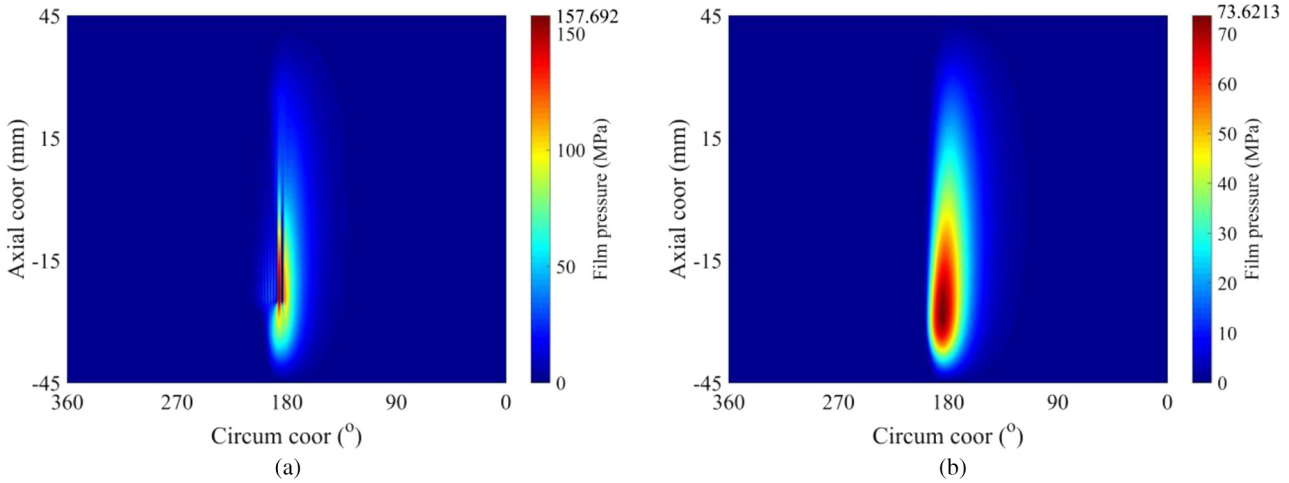

Fig. 10. (a) Film pressure of No. 5 test, (b) Film pressure of reference case 5.

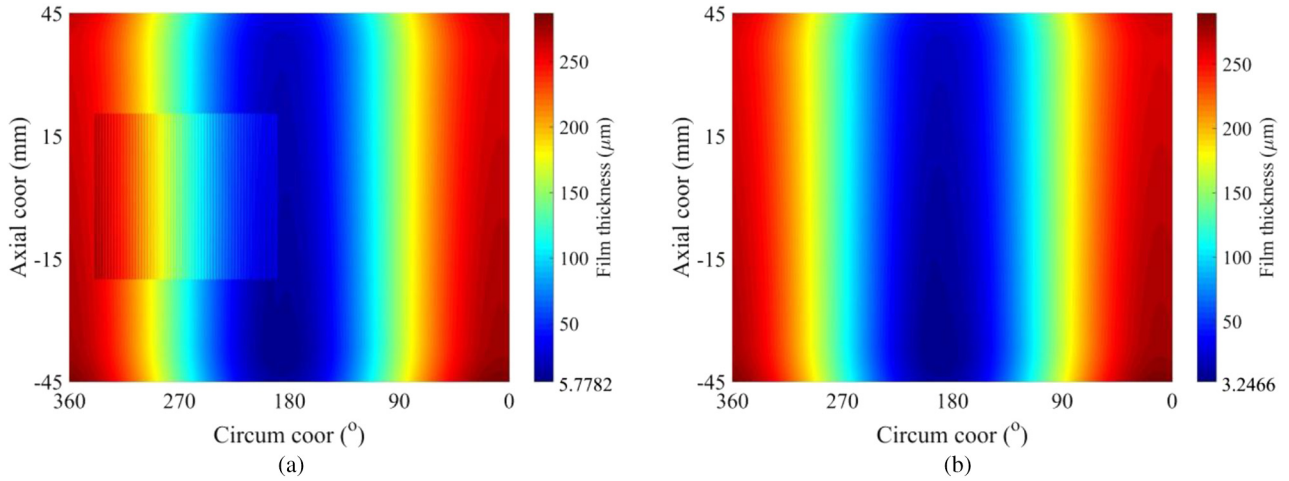

Fig. 11. (a) Film thickness of No. 15 test, (b) Film thickness of reference case 15.

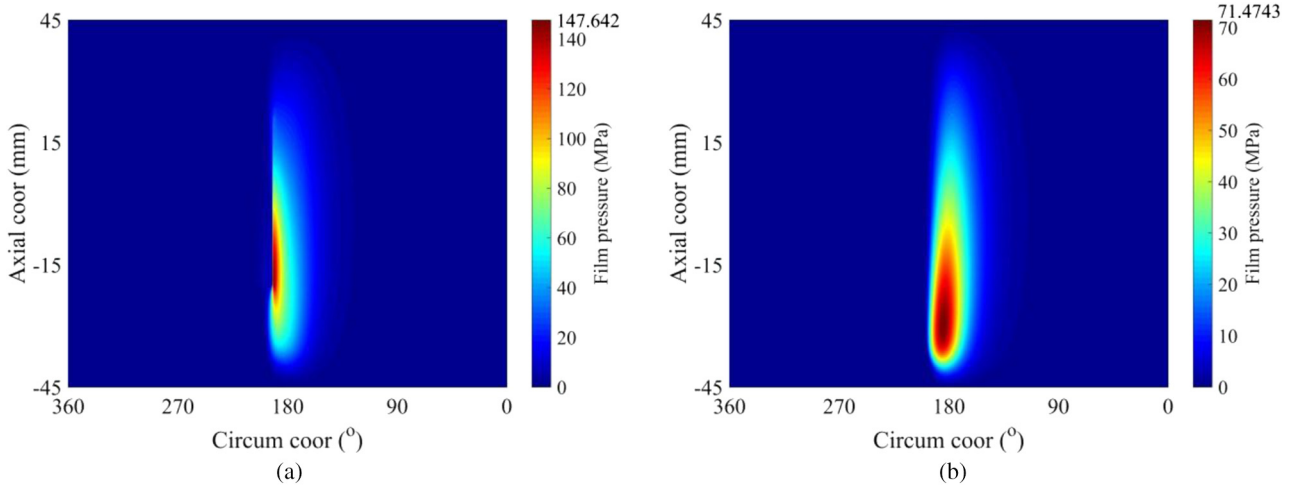

Fig. 12. (a) Film pressure of No. 15 test, (b) Film pressure of reference case 15.

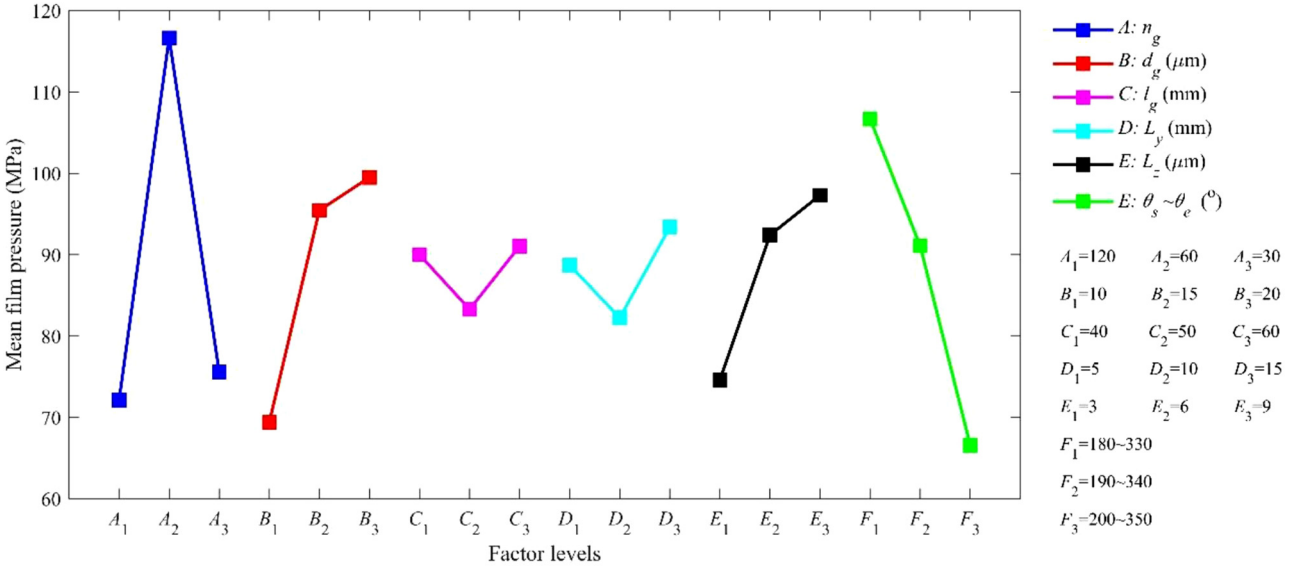

Fig. 13. Main effect plots of $P_{\max}$ (MPa).

carrying capacity. However, this combination does not exist in orthogonal table and another computation is conducted, denoted as No. 19 test. The results of this test are $P_{\max} = 64.0170$ MPa and $P_f = 4105.1540$ W, respectively, and $P_{\max}$ of all 19 tests are illustrated in Figure 14. It can be seen the No. 8 test, i.e., groove number 30, depth 15 μm, length 60 mm, axial width of dpp 10 mm, radial height of dpp 3 μm, and location 200°–350°, gives a maximum load carrying capacity, with only 4.69% increases of $P_{\max}$ than that in pp case.

Table 8 lists the results of ANOVA for load carrying capacity ($P_{\max}$). The columns represent the sources, degrees of freedom (*DF*), sum of squares (*SS*), mean of squares (*MS*), *F*-values, and $F_{0.05}(2, 5)$. Table 8 shows the groove number n_g, location θ_s–θ_e and depth d_g are the significant factors at 95% confidence level as their *F*-values are greater than $F_{0.05}(2, 5)$. The percentage contributions (*PCR*) of all factors are also given in Table 8, which shows the groove number n_g is the most important factor whose percentage contribution is 38.66%, followed by location θ_s–θ_e and depth d_g, whose percentage contribution are 25.78% and 16.85%.

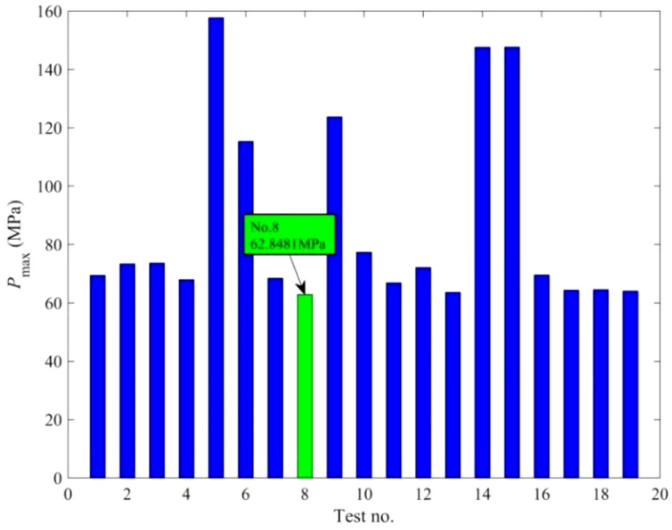

Fig. 14. $P_{\max}$ of all 19 tests.

The effects of six factors on the friction loss (P_f) are illustrated in Figure 15. It is clearly that Figure 15 suggests the optimal parameters combination is in the No. 6 test, i.e., groove number 60, depth 20 μm, length 60 mm, axial width of dpp 5 mm, radial height of dpp 3 μm, and location 190°–340°, which gives a minimum friction loss. The P_f of all 19 tests are illustrated in Figure 16, which also confirms the No. 6 test gives a minimum friction loss, 3643.9945 W, with 11.78% decrease than that in pp case.

Table 9 lists the results of ANOVA for friction loss (P_f), which shows the groove number n_g, depth d_g, axial width of dpp L_y, radial height of dpp L_z and location θ_s–θ_e are the significant factors at 95% confidence level. The percentage contributions of all factors are also given in Table 9, which shows the groove number n_g is the most important factor whose percentage contribution is 33.45%, followed by the location θ_s–θ_e, depth d_g, axial width of dpp L_y and radial height of dpp L_z whose percentage contributions are 21.57%, 21.00%, 11.39% and 8.04% respectively.

Note the interactions between factors are not considered in. In fact, the interactions can be neglected if the orthogonal table is reasonably designed. The ANOVA shows that, compared with the six factors, the *PCR* of errors are small, 6.62% of $P_{\max}$ and 2.70% of P_f, which indicates the interactions hidden in error are very limited. It can be found the interactions are also neglected in literatures [17–19].

From the above analysis, it can be observed the No. 8 test gives a maximum load carrying capacity while the No. 6 test gives a minimum friction loss. To find an optimal configuration, the grey relational analysis (GRA) method is used for this multiobjective optimization [19]. The main steps of GRA are listed as follows:

Step 1: Solution for normalized sequence.

As the optimization objectives are increasing load carrying capacity (smaller $P_{\max}$) and reducing friction loss (smaller P_f), the "the-smaller-the-better" criterion is used to normalize the orthogonal test results between 0 and 1, as shown below

$$X_i^*(k) = \frac{\max(x_i(k)) - x_i(k)}{\max(x_i(k)) - \min(x_i(k))} \tag{27}$$

where the $X_i^*(k)$ is the normalized sequence, $x_i(k)$ the sequence of $P_{\max}$ or P_f, $k = 1, 2$ (1 for $P_{\max}$ and 2 for P_f), and $i = 1, 2, \ldots, 19$ (test No.).

Table 8. ANOVA for $P_{\max}$.

Sources	*DF*	*SS*	*MS*	*F*-value	$F_{0.05}(2,5)$	*PCR* (%)
n_g	2	7356.50	3678.25	14.59	5.79	38.66
d_g (μm)	2	3205.37	1602.69	6.36	5.79	16.85
l_g (mm)	2	212.53	106.26	0.42	5.79	1.12
L_y (mm)	2	375.24	187.62	0.74	5.79	1.97
L_z (μm)	2	1711.73	855.87	3.40	5.79	9.00
θ_s–θ_e(°)	2	4905.44	2452.72	9.73	5.79	25.78
Error	5	1260.16	252.03	–	–	6.62
Total	17	19027	–	–	–	

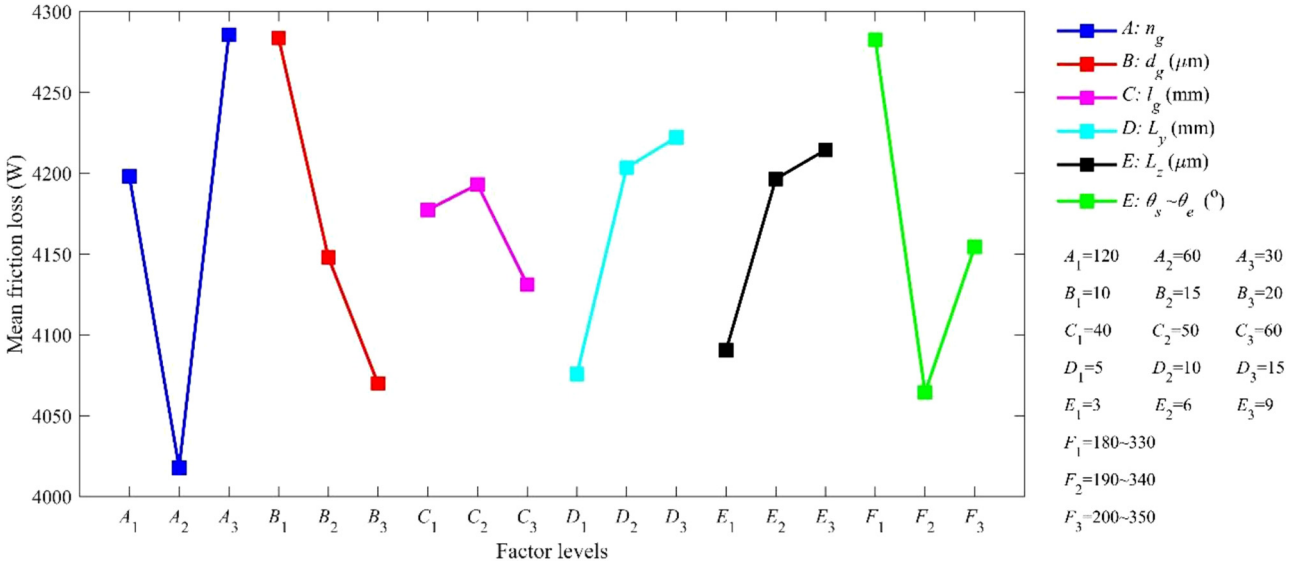

Fig. 15. Main effect plots of P_f (W).

Table 9. ANOVA for P_f.

Sources	*DF*	*SS*	*MS*	*F*-value	$F_{0.05}(2,5)$	*PCR* (%)
n_g	2	223725.89	111862.94	30.94	5.79	33.45
d_g (μm)	2	140416.45	70208.23	19.42	5.79	21.00
l_g (mm)	2	12403.84	6201.92	1.72	5.79	1.85
L_y (mm)	2	76153.33	38076.66	10.53	5.79	11.39
L_z (μm)	2	53770.19	26885.10	7.44	5.79	8.04
θ_s–θ_e(°)	2	144262.74	72131.37	19.95	5.79	21.57
Error	5	18078.14	3615.63	–	–	2.70
Total	17		–	–	–	

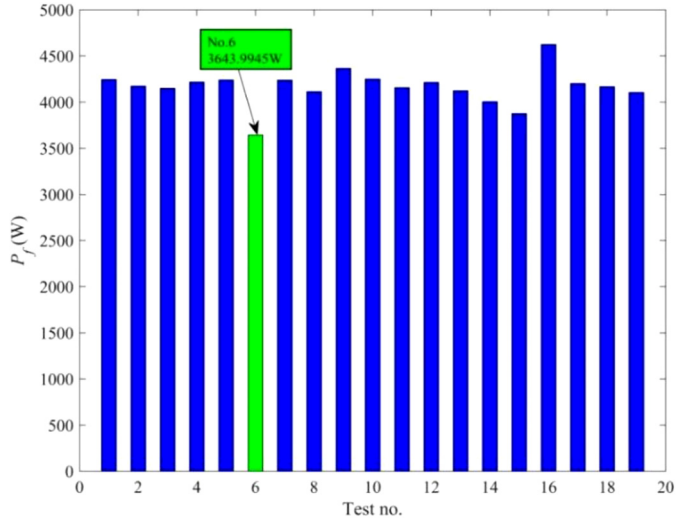

Fig. 16. P_f of all 19 tests.

Step 2: Solution for deviation sequence.

The deviation sequence, denoted as $\Delta_{0i}(k)$, is the absolute difference between the reference and normalized sequences, as shown below

$$\Delta_{0i}(k) = |X_0^*(k) - X_i^*(k)| \tag{28}$$

where $X_0^*(k)$ is the reference sequence.

Step 3: Solution for grey relational coefficient (GRC).

The GRC is calculated depending on the deviation sequence to describe the correlation between the reference and normalized sequences, as shown below

$$\xi_i(k) = \frac{\Delta_{\min} + \zeta\Delta_{\max}}{\Delta_{0i}(k) + \zeta\Delta_{\max}} \tag{29}$$

where $\Delta_{\min}$ and $\Delta_{\max}$ are the minimum and maximum values of $\Delta_{0i}(k)$, ζ the distinguishing factor between 0 and 1, here $\zeta = 0.5$, which means the increasing load carrying capacity and reducing friction loss are equally important.

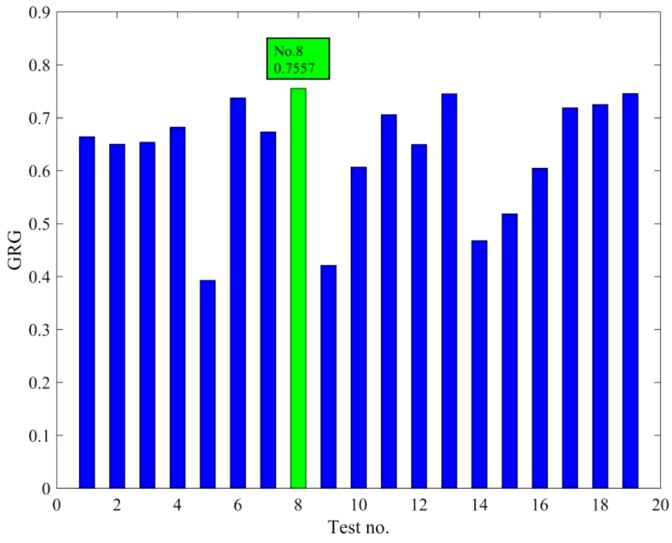

Fig. 17. GRGs of all 19 tests.

Step 4: Solution for grey relational grade (GRG).

The evaluation criteria for a multiobjective optimization is based on GRG, which is the mean of the GRCs, as shown in equation (30). The larger GRG means the parameter configuration approaches the optimal one.

$$\gamma_i = \frac{1}{n}\sum_{k=1}^{n}\xi_i(k). \tag{30}$$

Based on above four steps, the GRGs of all 19 tests are calculated and illustrated in Figure 17. It is observed the GRG of No. 8 test is the largest one, which means when both considering the load carrying capacity and friction loss, the parameters of No. 8 test, i.e., groove number 30, depth 15 μm, length 60 mm, axial width of dpp 10 mm, radial height of dpp 3 μm, and location 200°–350°, is the optimal parameters combination. In this case, the $P_{\max}$ is 62.8141 MPa and P_f is 4113.0399 W, with only 4.69% increase while 0.42% decrease than those in the pp case, and meanwhile the bushing edge wear is totally eliminated.

At last, it should be noted that the Taguchi and grey relational analysis methods gives the optimal parameters combination only limited to the preassigned parameter levels, which may miss the really optimal design. However, they are relatively simple and practicable, which facilitates the research of multi-parameters and evaluation of parameter effects.

5 Conclusions

In this study, based on Taguchi and GRA methods, a multiobjective optimization of journal bearing with double parabolic profiles and groove textures is researched under steady operating conditions. Following conclusions can be drawn from numerical results:

- Compared with plain profile, double parabolic profiles can eliminate bushing edge wear, and the stability of journal bearing can be also improved. However, it also has visible drawbacks, such as the reduced load carrying capacity (with 13.51% increase of $P_{\max}$) and increased friction loss (with 3.46% increase of P_f).
- Compared with double parabolic profiles, double parabolic profiles with proper groove textures can increase the load carrying capacity due to extra local pressure. Meanwhile, the friction loss also reduces with thicker oil film. The improper groove textures can deteriorate the performance as they will destroy continuous film pressure generation and increase friction loss.
- The main effects analysis based on orthogonal test results shows that, for load carrying capacity, the No.8 test gives a minimum $P_{\max}$, 62.8481 MPa, with only 4.69% increase than that in the case of plain profile. While for friction loss, the No. 6 test gives a minimum P_f, 3643.9945 W, with 11.78% decrease than that in the case of plain profile.
- The ANOVA shows that, for load carrying capacity, the groove number n_g and groove location $\theta_s-\theta_e$ are the significant factors at 95% confidence level, whose percentage contributions are 38.66%, 25.78%, 16.85% respectively. While for friction loss, the groove number n_g, groove location $\theta_s-\theta_e$, groove depth d_g, axial width of double parabolic profiles L_y and radial height of double parabolic profiles L_z are the significant factors at 95% confidence level, whose percentage contributions are 33.45%, 21.57%, 21.00%, 11.39%, and 8.04% respectively.
- The GRA shows that, the parameters combination of No. 8 test, i.e., groove number 30, groove depth 15 μm, groove length 60 mm, axial width of double parabolic profiles 10 mm, radial height of double parabolic profiles 3 μm, and groove location 200°–350°, is the optimal solution: $P_{\max}$ is 62.8141 MPa and P_f is 4113.0399 W, with only 4.69% increase while 0.42% decrease than those in the case of plain profile, meanwhile the bushing edge wear is eliminated.

The cavitation area of oil film determined by Reynolds boundary conditions may be less accurate than mass-conservative treatment, which is a limitation of this study. In future work, cavitation effects will be treated in mass-conserving way, and other optimization methods will also be tried for journal bearing to find the optimal texture design.

Nomenclature

D	Bearing diameter
B	Width of plain profile
d	Thickness of plain profile
L_y	Axial width of double parabolic profiles
L_z	Radial height of double parabolic profiles
h	Nominal film thickness
h_g	Nominal film thickness without elastic deformation
c	Radial clearance
e	Eccentricity of the midplane
φ	Attitude angle of the midplane
γ	Misalignment angle

δ_z	Variation clearance caused by double parabolic profiles
δ_{tex}	Variation clearance caused by groove textures
δ_e	Elastic deformation of bushing surface
E	Elastic modulus of the bushing
ν	Poisson's ratio of the bushing
μ	Viscosity of lubricating oil
p	Film pressure
$U_1,\ U_2$	Velocities of the two surfaces
σ	Standard deviation of combined roughness
ϕ_x,ϕ_y	Pressure flow factors
ϕ_s	Shear flow factor
h_T	Local film thickness
ω	Angular velocity of journal
P_{asp}	Asperity contact pressure
η	The number of asperities per unit area
β	The mean radius of curvature of the asperities
E	Composite elastic modulus
$F_{2.5}(h/\sigma)$	Gaussian distribution function
ϕ_f,ϕ_{fs},ϕ_{fp}	Shear stress factors
μ_{asp}	Boundary friction coefficient
f	Friction force
P_f	Friction loss
Q_1	Leakage flowrate from the front end plane
Q_2	Leakage flowrate from the rear end plane
Q	Total leakage flowrate
T_e	Effective temperature of lubricating oil
T_i	Inlet oil temperature
ρ	Density of lubricating oil
c_l	Specific heat of lubricating oil
$\mathbf{M_e}$	External moment
$\mathbf{M_t}$	Resultant moment
$\mathbf{M_{oil}}$	Hydrodynamic moment
$\mathbf{M_{asp}}$	Asperity contact moment
$M_{ex},\ M_{ez}$	External applied moment along the x and z axes
$M_{tx},\ M_{tz}$	Resultant moment along the x and z axes
$M_{oilx},\ M_{oilz}$	Hydrodynamic moment along the x and z axes
$M_{aspx},\ M_{aspz}$	Asperity contact moment along the x and z axes
ω_s	Overrelaxation factor
ε_p	Allowable precision for the solution of film pressure
ε_t	Allowable precision for the solution of the effective temperature
ε	Eccentricity ratio of the midplane
M_e	Amplitude of external moment
M_t	Amplitude of resultant moment
ω_φ	Correction factor of φ
ω_ε	Correction factor of ε
ω_γ	Correction factor of γ
$err_{xz},\ err_M$	Allowable precision for the calculation of load equilibrium
σ_b	Standard deviations of the roughness of the bearing surface
σ_j	Standard deviations of the roughness of the journal surface
$n_\theta,\ n_y$	Numbers of nodes along the circumferential and axial direction
h_{min}	Minimum film thickness
P_{max}	Maximum film pressure
$P_{asp\ max}$	Maximum asperity contact pressure
w_g	Groove width
w_e	Groove gap
l_g	Groove length
n_g	Groove numbers
$n_{g\theta} \times n_{gy}$	Mesh of single groove
d_g	Groove depth
S_g	Total area of groove textures
DF	Degrees of freedom
SS	Sum of squares
MS	Mean of squares
$X_i^*(k)$	Normalized sequence of $P_{\max}$ or P_f
$x_i(k)$	Sequence of $P_{\max}$ or P_f
${X_0}^*(k)$	Reference sequence
$\Delta_{0i}(k)$	Deviation sequence
$\Delta_{\min},\ \Delta_{\max}$	Minimum and maximum values of $\Delta_{0i}(k)$
ζ	Weight of $P_{\max}$ or P_f
$\xi_i(k)$	Grey relational coefficient
γ_i	Grey relational grade

Abbreviations

pp	Plain profile
dpp	Double parabolic profiles
dppgt	Double parabolic profiles with groove textures
ANOVA	Analysis of variance
GRA	Grey relational analysis
GRC	Grey relational coefficient
GRG	Grey relational grade

This work is supported by the National Natural Science Foundation of China (51809057) and Fundamental Research Funds for the Central Universities (3072019CFM0302).

References

[1] C. Liu, B. Zhao, W. Li, X. Lu, Effects of bushing profiles on the elastohydrodynamic lubrication performance of the journal bearing under steady operating conditions, Mech. Ind. **20**, 207 (2019)

[2] H. Zhang, M. Hua, G. Dong, D. Zhang, K. Chin, A mixed lubrication model for studying tribological behaviors of surface texturing, Tribol. Int. **93**, 583–592 (2016)

[3] J. Ji, C. Guan, Y. Fu, Effect of micro-dimples on hydrodynamic lubrication of textured sinusoidal roughness surfaces, Chin. J. Mech. Eng. **31** (2018)

[4] C. Gu, X. Meng, D. Zhang, Y. Xie, Transient analysis of the textured journal bearing operating with the piezoviscous and shear-thinning fluids, J. Tribol. **139**, 051708 (2017)

[5] B. Manser, I. Belaidi, A. Hamrani, S. Khelladi, F. Bakir, Performance of hydrodynamic journal bearing under the combined influence of textured surface and journal misalignment: a numerical survey, Comp. Rend. Mécan. **347**, 141–165 (2019)

[6] R. Yu, W. Chen, P. Li, The analysis of elastohydrodynamic lubrication in the textured journal bearing, Proc. Inst. Mech. Eng. J **230**, 1197–208 (2016)
[7] Q. Lin, Q. Bao, K. Li, M.M. Khonsari, H. Zhao, An investigation into the transient behavior of journal bearing with surface texture based on fluid-structure interaction approach, Tribol. Int. **118**, 246–255 (2018)
[8] N. Tala-Ighil, M. Fillon, P. Maspeyrot, Effect of textured area on the performances of a hydrodynamic journal bearing, Tribol. Int. **44**, 211–219 (2011)
[9] N. Tala-Ighil, M. Fillon, A numerical investigation of both thermal and texturing surface effects on the journal bearings static characteristics, Tribol. Int. **90**, 228–239 (2015)
[10] A.B. Shinde, P.M. Pawar, Effect of partial grooving on the performance of hydrodynamic journal bearing, Ind. Lubric. Tribol. **69**, 574–584 (2017)
[11] X. Pang, J. Chen, S.H. Hussain, Numeric and experimental study of generalized geometrical design of a hydrodynamic journal bearing based on the general film thickness equation, J. Mech. Sci. Technol. **26**, 3149–3158 (2012)
[12] H. Zhang, M. Hafezi, G. Dong, Y. Liu, A design of coverage area for textured surface of sliding journal bearing based on genetic algorithm, J. Tribol. **140**, 061702 (2018)
[13] H. Zhang, Y. Liu, M. Hua, D. Zhang, L. Qin, G. Dong, An optimization research on the coverage of micro-textures arranged on bearing sliders, Tribol. Int. **128**, 231–239 (2018)
[14] C. Sinanoğlu, F. Nair, M.B. Karamış, Effects of shaft surface texture on journal bearing pressure distribution, J. Mater. Process. Technol. **168**, 344–353 (2005)
[15] C. Shen, M.M. Khonsari, Numerical optimization of texture shape for parallel surfaces under unidirectional and bidirectional sliding, Tribol. Int. **82**, 1–11 (2015)
[16] C. Gologlu, N. Sakarya, The effects of cutter path strategies on surface roughness of pocket milling of 1.2738 steel based on Taguchi method, J. Mater. Process. Technol. **206**, 7–15 (2008)
[17] C.Y. Chen, C.S. Liu, Y.C. Li, S. Mou, Geometry optimization for asymmetrical herringbone grooves of miniature hydrodynamic journal bearings by using Taguchi technique, Proc. Inst. Mech. Eng. J. Eng. Tribol. **229**, 196 (2014)
[18] Z.P. He, W.Q. Gong, Factors influence the lubrication characteristics investigation and optimization of bearing based on neural network, Ind. Lubric. Tribol. **68**, 369–385 (2016)
[19] A.B. Shinde, P.M. Pawar, Multi-objective optimization of surface textured journal bearing by Taguchi based Grey relational analysis, Tribol. Int. **114**, 349–357 (2017)
[20] M. Rades, Dynamic analysis of an inertial foundation model, Int. J. Solids Struct. **8**, 1353–1372 (1972)
[21] J. Sun, C.L. Gui, Z.H. Wang, Research on elastohydrodynamic lubrication of a crankshaft bearing with a rough surface considering crankshaft deformation, Proc. Inst. Mech. Eng. D **222**, 2403–2414 (2008)
[22] C.R. Lin, H.G.J. Rylander, Performance characteristics of compliant journal bearings, J. Tribol. **113**, 639–644 (1991)
[23] S.B. Glavatskih, M. Fillon, TEHD analysis of thrust bearings with PTFE-faced pads, in *Proceedings of2004 ASME/STLE International Joint Tribology Conference*, 2004
[24] K. Thomsen, P. Klit, A study on compliant layers and its influence on dynamic response of a hydrodynamic journal bearing, Tribol. Int. **44**, 1872–1877 (2011)
[25] N. Patir, H.S. Cheng, An average flow model for determining effects of three-dimensional roughness on partial hydrodynamic lubrication, J. Lubric. Technol. **100**, 12–17 (1978)
[26] N. Patir, M.S. Cheng, Application of average flow model to lubrication between rough sliding surfaces, J. Lubric. Technol. **101**, 220–229 (1979)
[27] J.A. Greenwood, J.H. Tripp, The contact of two nominally flat rough surfaces, Proc. Inst. Mech. Eng. **185**, 625–633 (1970)
[28] F. Lv, Z. Rao, N. Ta, C. Jiao, Mixed-lubrication analysis of thin polymer film overplayed metallic marine stern bearing considering wall slip and journal misalignment, Tribol. Int. **109**, 390–397 (2017)
[29] S. Wen, P. Huang, Principles of Tribology, Fourth Edition, Tsinghua University Press, Beijing (2012)
[30] J. Ferron, J. Frene, R. Boncompain, A study of the thermohydrodynamic performance of a plain journal bearing comparison between theory and experiments, J. Lubric. Technol. **105**, 422–428 (1983)
[31] D.C. Montgomery, Design and Analysis of Experiment, Sixth Edition, John Wiley & Sons, Inc., Singapore (2005)

Cite this article as: C. Liu, N. Zhong, X. Lu, B. Zhao, A multiobjective optimization of journal bearing with double parabolic profiles and groove textures under steady operating conditions, Mechanics & Industry **21**, 305 (2020)